# Metallic Architectures from 3D-Printed Powder-Based Liquid Inks

*Adam E. Jakus, Shannon L. Taylor, Nicholas R. Geisendorfer, David C. Dunand, and Ramille N. Shah**

**A new method for complex metallic architecture fabrication is presented, through synthesis and 3D-printing of a new class of 3D-inks into green-body structures followed by thermochemical transformation into sintered metallic counterparts. Small and large volumes of metal-oxide, metal, and metal compound 3D-printable inks are synthesized through simple mixing of solvent, powder, and the biomedical elastomer, polylactic-co-glycolic acid (PLGA). These inks can be 3D-printed under ambient conditions via simple extrusion at speeds upwards of 150 mm $s^{-1}$ into millimeter- and centimeter-scale thin, thick, high aspect ratio, hollow and enclosed, and multi-material architectures. The resulting 3D-printed green-bodies can be handled immediately, are remarkably robust, and may be further manipulated prior to metallic transformation. Green-bodies are transformed into metallic counterparts without warping or cracking through reduction and sintering in a $H_2$ atmosphere at elevated temperatures. It is shown that primary metal and binary alloy structures can be created from inks comprised of single and mixed oxide powders, and the versatility of the process is illustrated through its extension to more than two dozen additional metal-based materials. A potential application of this new system is briefly demonstrated through cyclic reduction and oxidation of 3D-printed iron oxide constructs, which remain intact through numerous redox cycles.**

## 1. Introduction

From the early Copper Age several millennia ago, to the beginning of the Steel Age in the 19th century, our capacity to access and manipulate metals has created the foundation for the modern world. Today, metal structures are ubiquitous—from the tallest skyscrapers to the most elegant of jewelry—that we often forget much of it originated from metal containing ores, comprised of metal compounds, including oxides, reduced at high temperature into liquid metal and cast into ingots. Powder metallurgy provides an alternate approach to metal forming. Traditional powder metallurgy utilizes metal powders that are shaped and compacted into dense metallic objects through hot isostatic pressing[1] or dynamic compaction.[2] An alternative, indirect approach is to first fabricate objects of the desired architectures from metal precursors, such as metal oxides, and then thermochemically reduce and sinter them to form metallic counterparts,[3–6] including porous, cellular architectures that cannot be formed via direct metal casting.

Among the many established approaches for using metallic powders to create metallic architectures directly, there have been several previous examples that utilize the general approach of creating metal oxide powder objects and transforming them into disordered metallic foams[5–8] and linear cellular architectures.[3,4,9] In these instances, powder-based, metal-oxide green bodies are created and subsequently thermochemically reduced and sintered at elevated temperatures in reducing atmosphere (e.g., $H_2$ gas) to produce metallic structures with water vapor as a byproduct. Although effective in producing metallic objects, metal and metal oxide green body fabrication through traditional methods such as freeze-casting[7,8] and die extrusion[3,4] do not permit complex, fully user-defined, 3D architectures to be readily created. This is not only because designing and machining molds and dies for freeze-casting and extrusion is a time consuming, expensive process that does not lend itself to rapid, iterative design, but also because freeze-casting and extrusion parameters are highly geometry and material dependent.

Additive manufacturing (AM) and 3D-printing approaches offer the potential to achieve a much greater degree of design

Dr. A. E. Jakus, S. L. Taylor, N. R. Geisendorfer, Prof. D. C. Dunand, Prof. R. N. Shah
Department of Materials Science and Engineering
McCormick School of Engineering
Northwestern University
Evanston, IL 60208, USA
E-mail: ramille-shah@northwestern.edu
Dr. A. E. Jakus, S. L. Taylor, N. R. Geisendorfer, Prof. R. N. Shah
Simpson Querrey Institute for BioNanotechnology
Northwestern University
Chicago, IL 60611, USA
Prof. R. N. Shah
Department of Biomedical Engineering
McCormick School of Engineering
Northwestern University
Evanston, IL 60208, USA
Prof. R. N. Shah
Department of Surgery
Comprehensive Transplant Center
Feinberg School of Medicine
Northwestern University
Chicago, IL 60611, USA

**DOI: 10.1002/adfm.201503921**

and manufacturing flexibility and efficiency over freeze-casting and die-extrusion; however, the majority of current metal AM approaches still have numerous architectural and manufacturing limitations, in addition to being compatible with only a relatively narrow range of metals and alloys. Established metal AM methods require that metal powders be tightly packed into a powder bed, and then selectively sintered or melted layer-by-layer via precision application of a laser or electron beam.[10] Once complete, the part is removed from the surrounding loose powder and thoroughly cleaned of excess unsintered, and partially sintered powders. While the application of laser and electron beams for particle fusion restricts these methods to metallic powders that can be rapidly sintered and melted, the very nature of the powder bed process also prevents numerous, potentially advantageous structures from being produced, including enclosed, hollow, and tightly porous architectures. Additional deficiencies include the need for expensive, energy-intensive equipment, slow build rates, significant thermal gradients during fabrication (which can result in undesirable microstructures and local warping), excessive oxidation or contamination of powder before or after sintering, poor surface-finish, and warped final parts.[11]

Although not practical for all metallic systems, including those that cannot be effectively reduced, metal oxide powders offer a number of advantages over metallic powders, including reduced cost, availability in submicrometer sizes, and lack of reactivity and pyrophoricity.[11] However, due to their exceptionally high melting points (often several times that of their metal counterparts) they cannot be effectively sintered using applied energy beams. Williams et al.[11] attempted to address this shortcoming by utilizing a powder bed based inkjet binding AM technique to create metal oxide green bodies. After careful extraction from the powder bed and removal of excess powder, the green bodies were thermochemically reduced and sintered to produce metallic objects. However, because this was a powder-bed process, it still suffered from numerous processing limitations, including suboptimal powder packing, which ultimately negatively impacted the final metal density, surface finish, and overall quality of the final metal.

Others have attempted to address the architectural and practical weaknesses of powder-bed AM methods with liquid-extrusion-based 3D-printing, such as direct ink writing (DIW), which utilizes inks comprised of organic solvents, polymer, and suspended powders. This technique has previously been used to 3D-print structural,[12] conducting,[13] optical,[14] and biomedical[15,16] materials. One variant of the DIW method utilizes particle-based inks, which harden upon extrusion as a result of the rapid evaporation of comprising solvent and subsequent precipitation of a binding polymer.[17] The result is an architecture comprised of struts consisting of polymer-bound powder. Ahn et al. previously demonstrated that liquid-based $TiH_2$ ink suspensions, could be printed into 2D sheets, which, after wetting with solvents, could be folded and otherwise manipulated to create 3D $TiH_2$ objects which could be thermally decomposed to create partially sintered titanium metal.[18,19] Although this process was successful, the authors noted that it was difficult to produce many layered, high-aspect ratio objects, as well as unsupported, overhanging architectural features due to sagging of the inks under their own weight and lengthy solidification time. There was also a narrow window of time in which the printed sheets could be effectively manipulated to form 3D structures.[18]

A new advanced manufacturing approach is needed to overcome the significant material and architectural limitations of the previously mentioned AM and 3D-printing methods to enable the economical and consistent fabrication of complex metallic architectures that could not be formed using traditional or existing manufacturing methods. In this work, we introduce a new, highly versatile process that overcomes the material, architectural, technical, and practical limitations of current metallic AM and 3D-printing approaches. Using a new formulation of powder-based liquid inks comprised of a broad range of metal oxide, metal, and other metal compound powders, we illustrate that an extensive variety of architectures and materials can be rapidly 3D-printed and thermochemically processed to consistently yield intricate, pure, and alloyed metallic counterparts without warping or cracking. Taking advantage of the structural consistency upon thermochemical transformation, we also demonstrate that metallic architectures derived from 3D-printed oxide constructs can by cyclically oxidized and reduced, transforming repeatedly between oxide and metal, which is an enabling feature for emerging technologies such as iron-air batteries.[20–22]

## 2. Results and Discussion

Metallic architectures in this work are formed from metal, metal oxide, and other powders through the generic scheme illustrated in **Figure 1**. The inks are comprised of three main components: (i) metal-based powder(s), (ii) polylactic-*co*-glycolic acid (PLGA), an elastomer derived from biologically synthesized lactic and glycolic acid, and (iii) a previously reported tri-solvent mixture comprised of dichloromethane (DCM), dibutyl phthalate (DBP), and 2-butoxyethanol (2-Bu).[17,18] The resulting inks are essentially high volume fractions of powders suspended in a solvent mixture containing the dissolved elastomer, PLGA. Although widely used in the biomedical community as a biodegradable and biocompatible elastomer,[17,23] PLGA has never previously been used as a binder for these types of powder systems. Metal oxide inks are synthesized by creating a mixture of 2-Bu and DBP (2:1 by mass) with added DCM to which metal oxide powders are dispersed by stirring or shaking. This suspension is then combined with a solution of PLGA dissolved in DCM. The relative volume ratio of powder(s) to PLGA is 7:3 for the objects presented in this work, unless stated otherwise. DCM is initially present in excess to promote homogenous mixing of the components. The resulting preink is periodically stirred in an open container to allow excess DCM to evaporate until a low shear stress viscosity of 30–35 Pa s is achieved. The inks may then be 3D-printed immediately or stored in sealed glass bottles for later use.

Due to the simple mixing nature of the ink synthesis, batches as small as a few milliliters or as large as many liters (**Figure 2**A and Figure S1, Supporting Information) can be produced in a matter of hours. Additionally, because this process is physical rather than chemical in nature, a wide variety of metal oxide, metal, or metal compound inks can be produced through



*Adv. Funct. Mater.* **2015**,
DOI: 10.1002/adfm.201503921

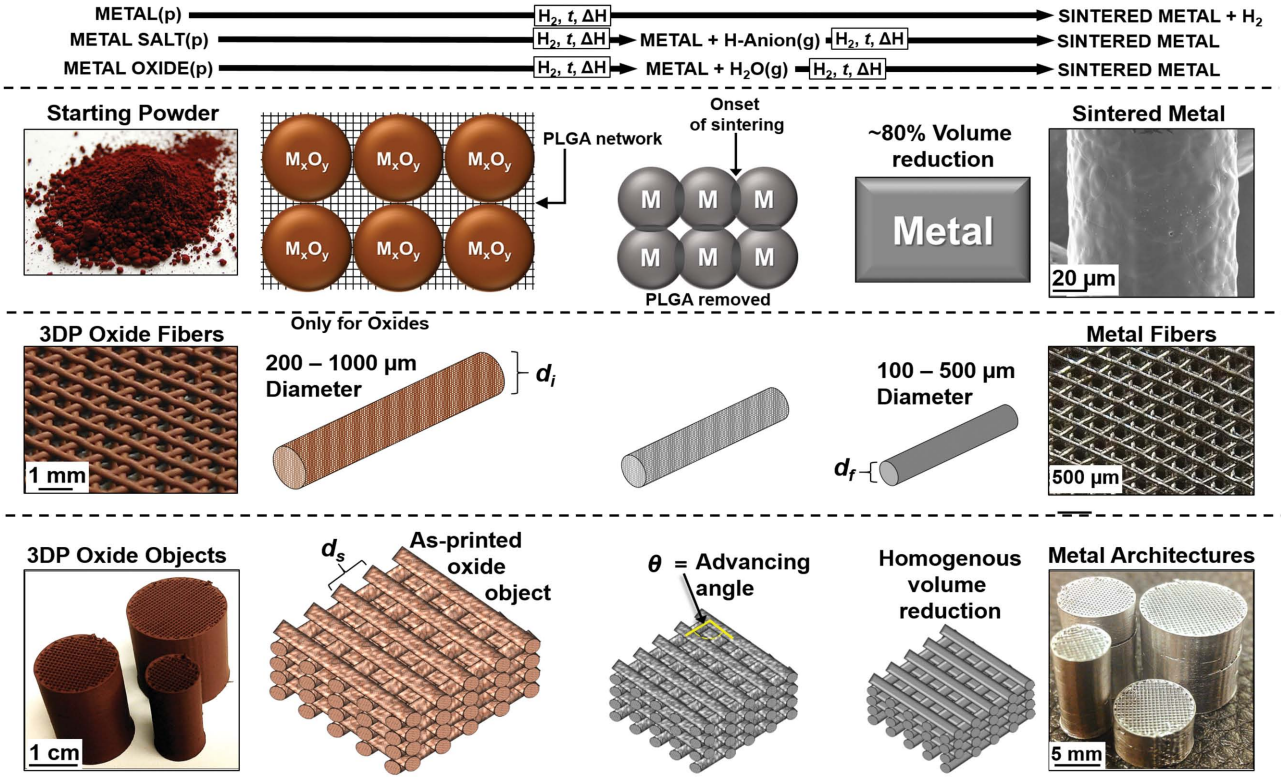


**Figure 1.** Particle-laden inks (comprised of metal, metal oxide, or metal compound powders) are extruded as a high viscosity liquid and immediately harden into 1D solid struts. A series of struts make up a single 2D layer of the final 3D cellular object which can be comprised of hundreds of layers. Through $H_2$ thermochemical reduction, the powder comprising the struts, layers, and ultimately the entire object, is reduced and sintered to form the final metallic (M) architecture, conserving the as-printed geometry but undergoing significant volume reduction. Metallic, metallic salt, or other metal compounds (carbides, nitrides, chlorides, etc.) powders may also be used in place of metal oxides ($M_xO_y$). Metallic powders will not undergo reduction, but will sinter, with $H_2$ acting as a protective gas, preventing oxidation or other metal reactions at elevated temperatures. Metallic salts will reduce in a similar manner to oxides, but will yield respective hydrogenated-anion vapor rather than water vapor, as in the case of oxides.

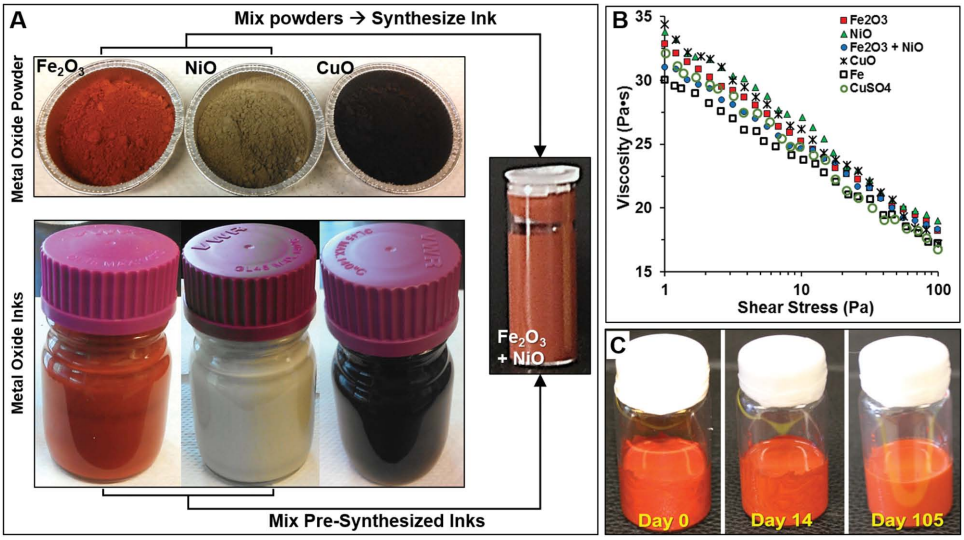


**Figure 2.** A) Metal oxide, metal, and other metal compound inks are produced by combining the respective powders with the tri-solvent mixture containing the appropriate volume of the dissolved elastomer, PLGA. Distinct powders can be used to make distinct particle inks, such as $Fe_2O_3$, NiO, and CuO. Compound inks, comprised of multiple powder types, such as that containing $Fe_2O_3$ and NiO (3:1 by mass elemental Fe:Ni) can be synthesized by either (1) creating an ink from a mixture of powders or (2) mixing previously synthesized inks in the appropriate quantities in a similar manner to mixing paint colors. B) Regardless of the powder comprising the ink, the rheological shear thinning behavior is the same provided that the composition is 7:3 by volume powder:PLGA. C) Photograph series of $Fe_2O_3$ ink illustrating that the ink does not settle out or observably separate over the course of 105 d.

simple substitution of the constituent powder(s) (Figure 2A). Multi-oxide inks may be synthesized through direct mixture of dry powders prior to ink synthesis, or through direct mixing of independently synthesized inks, similar to mixing paints to produce new colors. Regardless of composition, all inks exhibit the same shear thinning rheological behavior (Figure 2B), permitting them to be extruded through orifices as fine as 200 µm without clogging. Although the ultimate lifetime of the inks has yet to be determined, we have observed that 7:3 $Fe_2O_3$ inks that had been prepared one year prior can be 3D-printed without complications. This demonstrates that the inks have an extended shelf-life, a requirement for practical industrial applications. Even after 105 days, there is no apparent settling or separation of ink components (Figure 2C). However, similar to household paints, if settling does occur over longer periods of time, one need only to homogenize the ink via stirring or shaking prior to use. Additionally, unlike powder bed methods, which require extensive time and effort to exchange materials within a single instrument, the particle inks are cartridge-based; disposable cartridges containing distinct materials can be removed and loaded as needed in a matter of seconds. Furthermore, because this is a solid free-form fabrication process (unlike powder bed AM methods) constructs do not need to be cleaned of excess material upon completion.

As mentioned previously, due to purely physical interactions of powders with the solvents and polymer, this process is primarily independent of powder chemistry, and can be applied to metallic as well as other metal compound powders, such as metal sulfates, chlorates, carbonates, nitrates, pnictides, chalcogenides, halogenides, etc., with no significant difference in ink rheological properties (Figure 2B). When comprised of metallic powders, the same scheme as illustrated in Figure 1 holds true, minus the initial reduction step and without $H_2O$ as a byproduct, where $H_2$ gas in this instance acts to protect the metal from further oxidation during sintering. Metal compounds, including salts, will undergo both reduction and sintering in a similar manner to oxides, but will generate the corresponding acidic vapor ($H_2SO_4$, HCl, $H_2CO_3$, $HNO_3$, etc.) rather than $H_2O$.

Upon extrusion of the ink, the DCM rapidly evaporates, resulting in a solid-like, self-supporting fiber or strut. The remaining two solvents, DBP and 2-Bu, remain present in sufficient quantities to enable contacting struts to fuse, enabling large structures to be rapidly fabricated (Video S1, Supporting Information) and immediately handled. The resulting objects, despite being comprised of majority powder, are remarkably robust; they exhibit polymer-like mechanical properties, and are capable of undergoing upward of 100% tensile strain before failure (**Figure 3**A,B). Similar to the rheological consistency between distinct particle inks, the mechanical properties of 3D-printed oxides are also consistent with each other and appear to be independent of oxide chemistry (Figure 3C). Under compression, even objects comprised of as much as 9:1 oxide-to-polymer by volume do not catastrophically fail, but

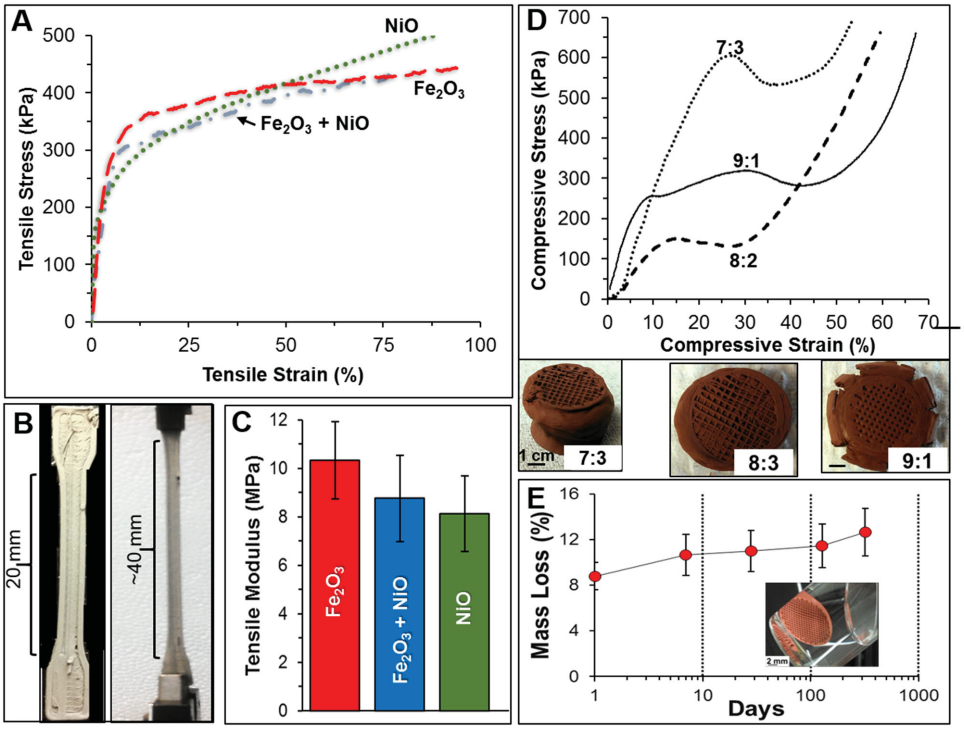


**Figure 3.** A) Representative tensile stress–strain curves for 3D-printed $Fe_2O_3$, NiO, and mixed $Fe_2O_3$ + NiO (3:1 by mass Fe:Ni) specimens. B) Photograph illustrating 3D-printed NiO tensile specimen before (left) and during (right) extension to nearly 100% strain with no necking. C) Tensile modulus of 3D-printed metal oxide materials. No statistically significant differences were observed. D) Uniaxial compressive stress–strain curve from 7:3, 8:2, and 9:1 3D-printed $Fe_2O_3$ cylinders. Cylinders were 1 cm diameter, 2 cm tall, and were defined by a 90° angle between adjacent layers and ≈70% open porosity; photos of final deformed specimens are shown below (D). E) Mass loss of 7:3 $Fe_2O_3$ sample as a function of days after being placed in water. Initial mass loss is due to excess solvents being removed by the water. Inset shows $Fe_2O_3$ cylinder six months after being placed in water.



*Adv. Funct. Mater.* **2015**,
DOI: 10.1002/adfm.201503921

rather, plastically deform (Figure 3D). Like the 7:3 inks, both 8:2 and 9:1 powder:PLGA inks can be 3D-printed once they have attained a viscosity of 30–35 Pa·s. However, unlike the 7:3 inks, which rarely clog fine (200 µm) nozzles, clogging frequency significantly increases with 8:2 and 9:1 inks, and renders them less effective for consistent use. Additionally, 3D-printed oxide architectures are stable when submerged in water (Figure 3E), initially undergoing 9% mass reduction due to residual solvents being removed, the printed objects only lose an additional 3%–4% mass over the course of 320 d. This is because PLGA is much more environmentally stable than commonly used water-soluble binders such as polyethylene glycol (PEG) or polyvinyl alcohol (PVA),[24] and indicates that the particle inks could potentially be coprinted with water-soluble support materials if needed.

Similar to previously described inks,[18] 2D sheets comprised of several layers can be created and manipulated via rolling, folding (origami), cutting, folding and cutting (kirigami), and fusing[18,19] (**Figure 4**A). However, unlike previously described inks, these sheets can be rapidly produced (Video S2, Supporting Information), handled immediately, and manipulated as long as one year after fabrication, without needing to rewet with solvent to impart flexibility. Most importantly, unlike previously described particle-based inks which require manipulation of 2D sheets to create 3D architectures, the particle-PLGA inks are far more versatile and can be directly, rapidly 3D-printed (at linear print speeds exceeding 150 mm $s^{-1}$) into many-layered, complex, hollow enclosed, high-aspect ratio structures (Figure 4B–D and Figure S2, Videos S3–S5, Supporting Information), with final metal fiber diameters as fine as 90 µm. Relative density of final metallic structures, which is primarily dictated by the user-defined fiber spacing prior to 3D-printing the object of interest, ranges from 0.1 to 0.7 (90%–30% structural porosity), illustrating that a wide range of relative densities (total porosity as well as designed porous architecture) can be rapidly incorporated into the structures through instant alterations to the digital design.

Independently printed parts may also be fused by applying ink with a syringe at points of contact. This approach can be used to create complex architectures that would otherwise be too difficult to 3D-print directly, such as an anatomically correct, hollow skull and spine derived from magnetic resonant imaging data (Figure 4E). This process is not only beneficial for creating architectures that may have features that cannot be 3D-printed directly, but may potentially be used for modular fabrication, whereby a relatively small printing platform can be used to produce units, which can be subsequently fused together, as needed, to create much larger end use parts. This holds true for all particle inks and constructs printed using this process (Figure 4F). Finally, objects 3D-printed from these inks have the additional advantage of being recyclable (Figure S3, Supporting Information). Scrap material, or objects that did not print correctly can be dried out and dissolved back into the appropriate volume of solvents, transforming them back into a 3D-printable ink.

Although the ink synthesis and 3D-printing parameters are independent of the powder, thermochemical reduction and sintering are not. Because of the differences in melting temperatures, self-diffusion coefficients, reduction thermodynamics and kinetics, volumetric change, and existence of suboxides

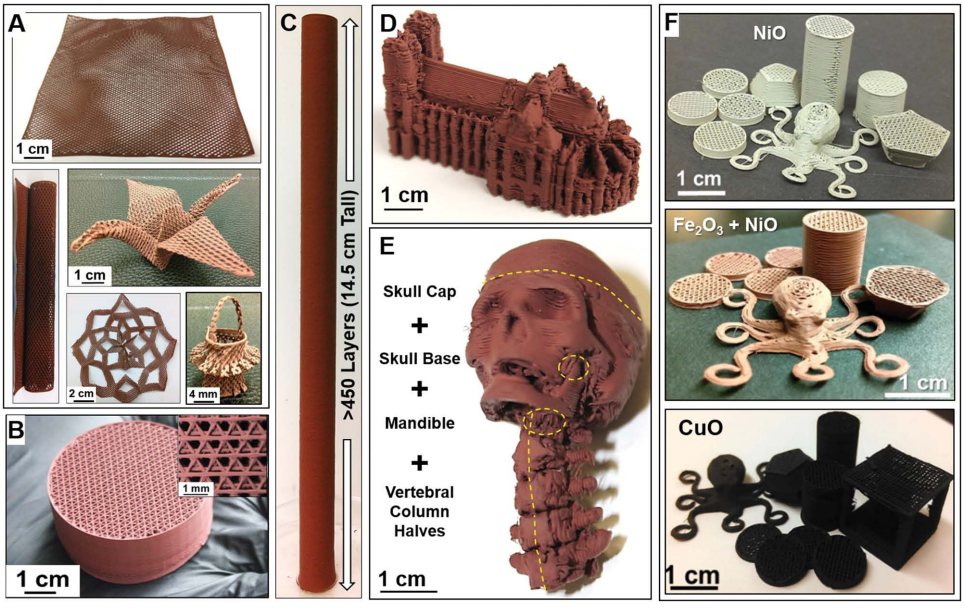


**Figure 4.** A) Photographs of three-layer 3D-printed $Fe_2O_3$ sheet, which can be rolled (into a tube), folded via origami (into a crane), folded and cut (kirigami; to make a snowflake), and folded, cut, and fused to make a Chinese lantern. B) $Fe_2O_3$ cylinder comprised of ≈250 180 µm thick layers (inset shows detail of internal structure). C) 3D-printed $Fe_2O_3$ 1 cm diameter, 14.5 cm tall, hollow cylinder comprised of more than 450 vertical layers (see Video S3, Supporting Information). D) Scale model of Notre Dame de Paris cathedral 3D-printed directly from $Fe_2O_3$ ink. E) Skull and attached upper spinal column 3D-printed from $Fe_2O_3$ ink using individual computed tomography (CT) data sets. Skull and vertebral column are hollow, and entire construct is comprised of five independently printed parts which were subsequently fused together through application of $Fe_2O_3$ ink. Dashed yellow lines indicate fused regions. F) Photographs of a variety of 7:3 NiO, $Fe_2O_3$ + NiO, and CuO 3D-printed objects.

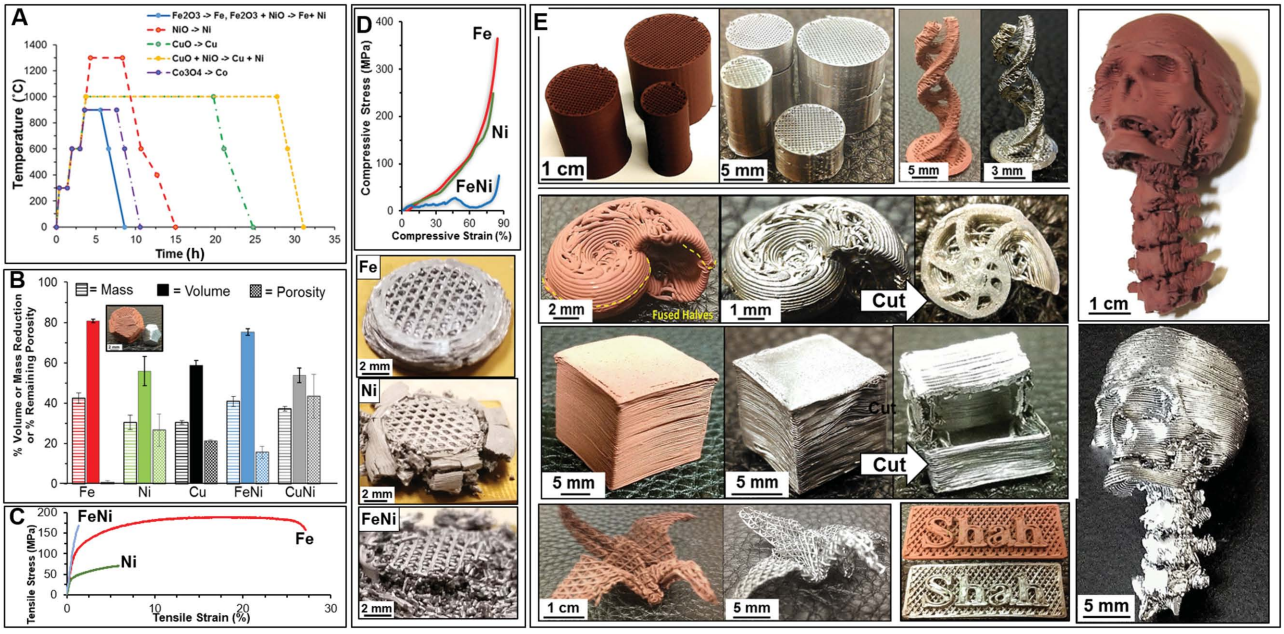


**Figure 5.** A) Furnace profiles, in flowing $H_2$ atmosphere, used to debind, reduce, and sinter the respective 3D-printed oxide systems. B) Relative average volume, mass reductions, and remaining porosity (within the metal, not the designed porosity) for each oxide-to-metal system. C) Representative tensile curves for metallic Fe, Ni, and Fe—Ni derived from respective reduced and sintered 3D-printed 7:3 metal oxide tensile specimens. D) Representative compression curves and corresponding post-testing photos of Fe, Ni, and Fe—Ni derived from respective reduced and sintered 3D-printed metal oxide cylinders. E) Photographs depicting 3D-printed $Fe_2O_3$ objects before (left or top) and after (right or bottom) reduction and sintering, including; cylinders (60%–70% porous), high-aspect ratio, organically curved DNA model, nautilus shell comprised of two independently printed and subsequently fused halves (cross section of cut sample shown on right), hollow box, origami crane, a letter plate, and the fused skull and spine originally displayed in Figure 4.

and metal compounds, the thermal treatment must be specifically tailored to the material. **Figure 5**A displays the time–temperature profiles used to achieve Fe, Cu, Ni, Co metal, and Fe—Ni and Cu—Ni alloy structures (**Figure 6** and Figure S6, Supporting Information) from their respective 3D-printed metal oxide green bodies. Initially, as the temperature increases to several hundred degrees Celsius, the PLGA decomposes and is removed from the structure. During this time, reduction of the comprising metal oxide powders to metal begins. As peak temperatures are reached, reduction and metallic sintering continue to occur simultaneously. For the alloy systems, such as Fe—Ni and Cu—Ni, this also results in substantial interdiffusion and alloying (Figure S7, Supporting Information). The end results are metallic objects that retain their original as-printed architectures (Figure 5E), but undergo significant mass and volume reductions (Figure 5B), which are independent of 3D-printed architecture, but highly dependent on composition as well as degree of sintering. Mass is reduced 30%–40% across all oxide–metal systems, corresponding to the removal of 30 vol% PLGA and loss of oxygen during reduction. Linear and volumetric reduction range from 40%–45% to 57%–80%, respectively, which is consistent with other thermochemically processed oxide structures.[11] These large volume reductions result from the increase in specific density (≈30%) upon oxide-to-metal reduction and interparticle space elimination via sintering.

Interestingly, despite such extreme volume changes, neither warping nor cracking are evident in the final metallic structures (Figure 5E). All structural and surface features are also maintained on the micrometer scale, where both user-defined lattice designs and unintentional printing artifacts are faithfully conserved (Figure S5, Supporting Information). Mixed oxide objects also successfully maintain their original architectures after chemical homogenization by interdiffusion (Figure S6, Supporting Information). Monolithic, high-aspect ratio, folded, fused, and even hollow, enclosed objects maintain their original architectures throughout the thermochemical reduction process (Figure 5E).

Although the exact mechanism governing this consistent, homogenous volume reduction is not entirely clear, we believe it is intimately connected with the compositional homogeneity throughout the structures. It must not be the case that binder burnout, reduction, and sintering occur sequentially but rather, in parallel to some degree. Residual carbonaceous matrix from the decomposing elastomer is likely still present as the metal oxide particles are reducing and sintering, acting as a temporary physical support for the particles, fibers, and overall structure, preventing warping, cracking, and other undesirable deformations. Another possible mechanism governing this phenomenon is particle jamming.[52,53] Aided by the condensation and solidification of the elastomer upon ink solidification, such high particle packing densities (Figure S1) in the green bodies permit the 3D-printed architectures to perfectly maintain their shapes even after the removal of the elastomer matrix. This is similar to packing wet sand to create self-supporting, arching structures, which are maintained, although mechanically unstable, even after the moisture evaporates. Although fragile without the matrix, the green-body architectures are



Adv. Funct. Mater. 2015,
DOI: 10.1002/adfm.201503921

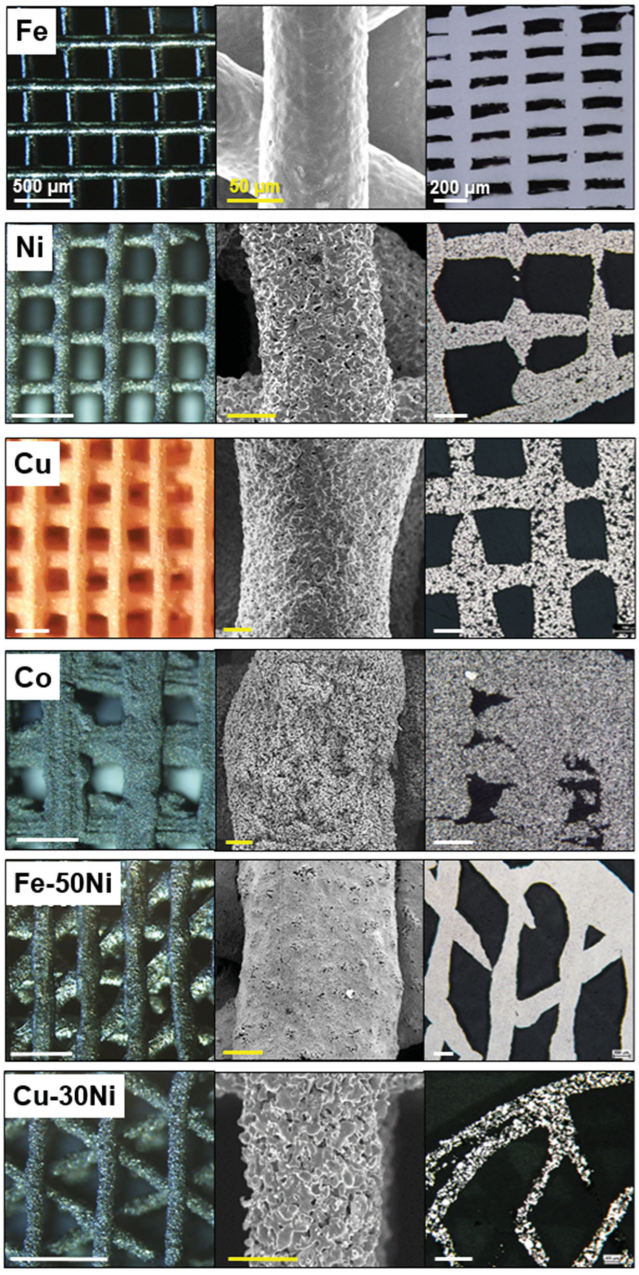


**Figure 6.** Representative examples of various ferrous and nonferrous metallic objects derived from 3D-printed 7:3 metal oxide:PLGA objects and corresponding SEM images, highlighting the surface structure of the metal struts, and metallographic cross-sectional images highlighting strut internal porosity. All scale bars for first, second, and third columns represent 500, 50, and 200 µm, respectively.

maintained until particles begin to sinter and are able to support the entire structure.

Beyond the obvious physical changes in appearance and size after transformation into metals, specimens also exhibit metallic mechanical properties, distinct from the polymer-like as-printed oxide counterparts (Figure 3). The mechanical properties of the metallic tensile and compression specimens are primarily dictated by their relative density postsintering (Figure 5B). Under tension (Figure 5C), metallic specimens derived from $Fe_2O_3$ exhibit behavior similar to pure iron, straining upward of 28% prior to failure and having an elastic modulus of 198 ± 45 MPa. Due to the large internal porosity, Ni fails at ≈5% strain, while Fe—Ni fails at less than 2%. Corresponding trends are observed during compression of 70% porous metallic cylinders derived from their respective oxides (Figure 5D and Video S6, Supporting Information), where iron is highly ductile, nickel exhibits some ductility, and Fe—Ni fails catastrophically.

Fe and Fe—Ni structures were near fully dense after their respective processing, but Ni, Cu, Co, and Cu—Ni struts did not fully densify (Figure 6 and Figure S7, Supporting Information). We note that the thermochemical treatment parameters, which may also include hydrogen gas flow rate and isothermal periods, have not been optimized to achieve full density for each of the metallic and alloy systems evaluated. Achieving fully dense struts in a single heat treatment would require the time–temperature profile for each metal and alloy system to be optimized. Alternatively, structures could undergo additional heat treating after initial reduction and presintering to tailor the resulting porosity and properties.

Although metal oxides have many advantages over metals as raw starting powders, including chemical stability, safety, reduced cost, and availability in submicrometer sizes, they do have several limitations, including the fact that not all oxides can be reduced via thermochemical treatment in hydrogen to produce metal. These include high stability metal oxides of aluminum, magnesium, tantalum, titanium, and others. In such instances, it is advantageous to create and 3D-print metallic inks and thermochemically process them accordingly. We illustrate that this process is exceptionally versatile (**Figure 7**) and can be readily extended to create a wide array of elemental metals, metal mixtures, and metal compound inks. These inks can be rapidly 3D-printed into many-layered porous architectures using tips as small as 200 or as large as 800 µm in diameter (Video S7, Supporting Information). It is also worth noting that this process appears to be independent of the powder density. Magnesium ($\rho$ = 1.74 g cm$^{-3}$) and tungsten ($\rho$ = 19.25 g cm$^{-3}$) inks exhibit the same 3D-printing characteristics, with no evidence of tungsten powders settling over the course of at least 4 d. Like the metal oxides, inks comprised of multiple metals, representative of desired alloy compositions, can also be produced and 3D-printed. Although it is certainly not a trivial task, thermal processing must be optimized for each composition to achieve adequate sintering, alloying, microstructure, and corresponding structural and functional properties. However, there exists a large body of established sintering knowledge and techniques that can guide future work on this processing and optimization[25–38] for each metal system and for the desired applications. An additional advantage to objects 3D-printed from metallic inks, depending on the application, is that they undergo significantly less volume reduction, ≈30% as opposed to 57%–80%, as a result of thermal processing (Figure S8, Supporting Information), relative to their 3D-printed oxide counterparts. This is certainly advantageous when large volume reductions may or may not be desired, and has the additional potential advantage of permitting volumetric shrinkage to be tailored between 30% and

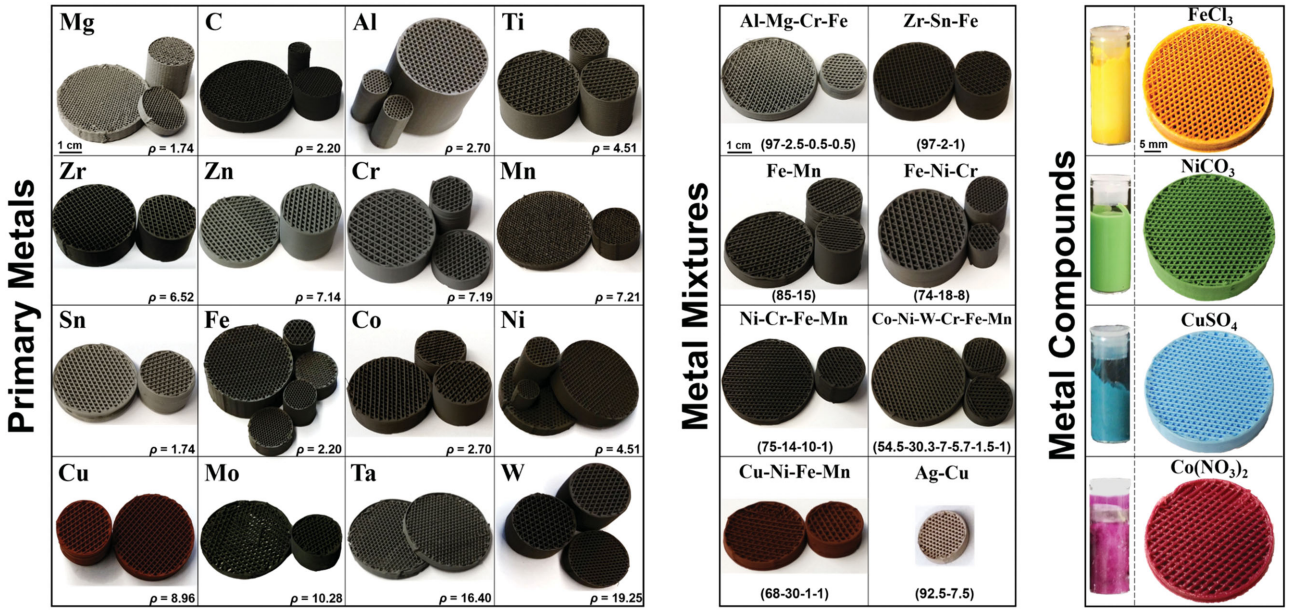


**Figure 7.** Photographs of green body cylinders (prior to thermochemical processing) 3D-printed from 7:3 metallic, metallic mixture (numbers are by mass), and nonoxide metallic compound inks (insets). Cylinders vary in diameter from 1 to 4 cm, and in height from 0.5 to 4 cm. Metal mixture inks were produced by mixing elemental powders in the appropriate mass ratios prior to ink synthesis.

80% by utilizing inks comprised of both metal and metal oxide (same metal) in the appropriate ratios.

Furthermore, due to the printing compatibility of all these inks, they are capable of being 3D-printed together into complex multimaterial structures (Figure S9, Video S8, Supporting Information). Determining the corresponding, optimal thermal treatments for such multimetal objects will be significantly more complicated than for single metal constructs due to differences in melting points, kinetics of reduction and sintering, and interdiffusivities of each of the metals. However, because of the ease of creating and 3D-printing inks comprised of numerous powders, including combined metals and metal oxides, it may be potentially possible to create multimetal constructs in which each printed component in the system sinters, shrinks, and otherwise thermochemically transforms at similar rates.

As a new means of metal manufacturing that expands both the types of metallic materials and 3D architectures that can be produced, this process has many potential applications. One such application is for manufacturing iron-air batteries. Due to its low cost and high energy efficiency, iron oxide powder is among the leading candidates for storing and creating pure hydrogen through the iron reduction/oxidation reaction ($Fe + H_2O = FeO + H_2$).[39,40] The produced hydrogen can then be consumed in a fuel cell with oxygen from the air to create electricity, and the process can be inverted (the fuel cell creates hydrogen that then reduces iron oxide to iron) thus creating a rechargeable iron-air battery with overall reversible reaction $Fe + ½O_2 = FeO$.[20–22] A key limitation to such solid-oxide flow batteries is the structural degradation, increasing with cycling, from sintering and/or pulverization of the Fe/FeO powders.[20,41–43] This degradation is primarily due to the large volume changes associated with the redox cycling (≈37% from Fe to FeO). Suitable Fe/FeO structures must have high open porosities to accommodate these volume changes and allow gas flow as well as high surface areas to promote rapid oxidation and reduction, making the 3D-printed and thermochemically treated iron architectures promising candidates.

Here, we demonstrate the application of the previously presented 3D-printed iron cellular architectures as potential $H_2$ reversible storage materials and structures for solid-oxide flow batteries. Reduced and sintered iron constructs, derived from 3D-printed $Fe_2O_3$, were subjected to cyclic oxidation in steam and reduction in hydrogen after which their structural integrity, mass change, and porosity were assessed (**Figure 8**). The printed architecture provides adequate space between the struts for the volume changes associated with the redox cycling (Figure 8A) and ensures structural stability against pulverization since the samples did not lose any mass over the course of ten redox cycles (Figure 8B). The extent of oxidation during each cycle decreases after the first few cycles due to a decrease in architectural porosity, and corresponding permeability, with time; however, the architectures remain sufficiently porous for gas ingress. The structures always fully reduced to metal after reduction. Cross sections of samples after the first oxidation and reduction steps (Figure 8C,D) show a significant amount of Kirkendall porosity. Metallographic examination of the samples after the final cycle showed significant sintering and choking of the printed channels. Optimization of the architecture, increased oxidation times, decreased operating temperatures (to ≈550–650 °C),[44,45] and the inclusion of alloying elements such as Al, Cr, Mo, and Ce to increase the stability and oxidation activity[20,21] should further improve architectural preservation during redox cycling.

Although the largest objects we present here are on the multi-cm scale, the scale limiting factors are the total volume capacity of the extrusion-based 3D-printer, the size of the hydrogen furnace, and the capacity for $H_2$ to react with and




DOI: 10.1002/adfm.201503921

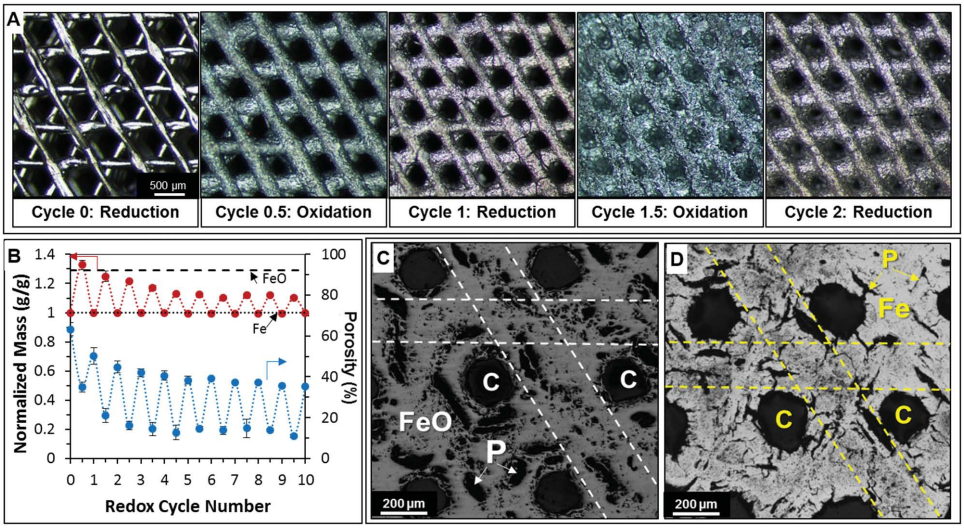


**Figure 8.** A) Top down images of 3D-printed Fe architectures after each of the first four half redox cycles. B) Plot of mass (normalized to the initial reduced and sintered iron mass) and porosity during the redox cycling experiments. C) Cross section of oxidized Fe structure after cycle 0.5 (oxidized). D) Cross section of reduced Fe structure after cycle 1 (reduction). In both (C) and (D), printed channels are labeled with C, Kirkendall pores are labeled with P, and one printed strut, from each of two printed layers, is outlined by a set of parallel dashed lines.

$H_2O$ vapor to exit from all oxide material in the structure. The capability of creating meter-scale objects using extrusion-based 3D-printers has already been demonstrated,[46] and large $H_2$ furnaces and additional reduction processes (such as electrolytic reduction) are already widely used in industry. Although we have been able to successfully 3D-print at speeds in excess of 150 mm $s^{-1}$ (maximum speed allowable by available hardware) using a single nozzle system, fabrication times could be further reduced by orders of magnitude using multinozzle, parallel printing systems.[47] Given the exceptional 3D-printing rates that could potentially be achieved, the limiting throughput factor may appear to be the extended lengths of time required for thermal processing. However, it should be noted that this approach is amenable to batch or continuous thermal processing, whereby many compositionally similar objects could be rapidly 3D-printed in series or parallel and collectively reduced and sintered in large volume furnaces under previously determined, optimal conditions. This approach would mirror many long established, high-throughput, consumer ceramics manufacturing methods.

## 3. Conclusions

We have demonstrated that diverse metallic architectures can be produced through 3D-printing of metal oxide and other powder-based liquid inks followed by thermochemical processing. This work lays the foundation not only for greatly expanding the variety of metals and alloys that can be additively manufactured but also other particle-based materials, such as ceramics and composites, as well as potentially yet-to-be-discovered advanced materials. It also demonstrates that the manufacturing shortcomings of the long established, energy-based and powder-bed AM and direct ink write 3D-printing platforms can be overcome through further "3D-ink" design and engineering. Although complete densification was not achieved for all metal systems illustrated here, material porosity, combined with tailored, wide interconnected porous channels, may be desirable for a number of applications, particularly those related to surface mediated reactions where both high specific surface area and rapid mass flow are required (e.g., batteries, heat exchangers, electrodes for die-sensitized solar cells, and catalyst substrates). Additionally, porosity is desirable for biomedical alloys intended for implants such as those based on Co,[48] where additional surface area not only accelerates biological integration[49] but also reduces the stiffness of the implant, mitigating stress shielding and long-term bone resorption surrounding the implant.[50] On the other hand, fully dense metal struts arranged in an open cellular network may be desirable for a number of light-weight structural[51] applications. The individual material flexibility enabled by this method, combined with the potential capacity to fabricate complex multi-metal and other multi-material constructs opens the door for exploring an extensive variety of structural, energy, and biomedical applications and devices that would otherwise not be technically or practically accessible with existing manufacturing methods.

## 4. Experimental Section

Oxide inks were synthesized through physical mixing by hand of (i) PLGA (85:15 PLA-PLG by mass) copolymer (Boehringer Ingelheim, Germany), (ii) metal oxide powders (1–5 μm, $Fe_2O_3$ from Sigma, NiO and CuO from American Elements, $Co_3O_4$ from Inframat Advanced Materials), and (iii) a 15:2:1 by mass mixture of DCM (Sigma), ethylene glycol butyl ether (Sigma), and dibutyl phthalate (Sigma)—0.9 g dibutyl phthalate was added for every 1 $cm^3$ metal oxide powder. Metal inks were synthesized from 1–10 μm or −325 mesh metallic powders (Alfa Aesar) and metal salt inks were synthesized from corresponding powders purchased from Alfa Aesar using the same processes as utilized for other inks. Powder to PLGA ratios of 7:3, 8:2, and 9:1 by volume were used. Inks were left open in a fume hood at room temperature, occasionally stirred by hand, and allowed to thicken via excess DCM evaporation to a viscosity of 30–35 Pa s, a process which

can take several hours, but varies depending on the volume of ink being produced. The powder component for $Fe_2O_3$ + NiO inks was created by physically mixing dry $Fe_2O_3$ and NiO powders to achieve an Fe-50 wt% Ni alloy after reduction and sintering. 7:3 CuO + NiO inks were created in a similar manner by mixing 7:3 CuO:NiO by mass to achieve a Cu-30 wt% Ni alloy after reduction and sintering. Mixed metallic inks were synthesized by physically mixing powders, in the as-stated weight ratios, via vortexing for ≈30 min prior to adding them to the tri-solvent mixture. Once suspended in the tri-solvent mixture, metal suspensions were further vortexed for ≈30 min prior to their addition to the PLGA-DCM solution, at which point they were thickened to 30–35 Pa s as described above.

All 7:3 inks were rheologically characterized using a Couette fixture with solvent trap (MCR Rheometer, Paar Physica) under rotational shear at interval stresses between 0 and 100 Pa.

All 3D-printed structures were fabricated using a 3D-BioPlotter (EnvisionTEC GmbH, Germany) at extrusion pressures ranging from 50 to 300 kPa. Linear printing speeds ranged from 5 to 150 mm $s^{-1}$. Digital 3D files for octopi, nautilus shell, Notre Dame, skull, and spine were obtained from the open-source site thingiverse.com. All other digital designs were created by the authors using EnvisionTEC software. Multimaterial objects were designed and printed using EnvisionTEC software and 3D-BioPlotter, respectively. Internal porosity for printed objects ranged from 20% to 80%, and was determined by the strut spacing, thickness, and internal porosity.

Tensile and compression tests on as-printed oxide objects were performed on an LF Plus mechanical tester (Lloyd Instruments), at extension and compression rates of 2 mm $min^{-1}$. Compression samples measuring 2 cm tall, 1 cm diameter, alternating perpendicular, oriented layered cylinders were 3D-printed using a nozzle with a 200 µm diameter tip. Tensile specimens were created by 3D-printing 7:3 oxide inks into solid parts conforming to EN ISO 527-2:1996, but with reduced dimensions (22 mm gauge length by 3.2 mm wide and 2.5 mm thick). Tensile and compression testing of metallic specimens derived from 3D-printed oxides (same geometries as those used for oxide mechanical testing, but dimensional reduction corresponding to particular metal system) was performed on an MTS Sintech 20G at extension and compression rates of 1 mm $min^{-1}$. Samples were imaged using both LEO 1525 and Hitachi S3400-II scanning electron microscopes (using carbon sputter coatings or osmium plasma-coating prior to imaging).

All 3D-printed samples were heat-treated in a hydrogen furnace (MTI Corporation GSL-1500X-50HG) using 99.999% pure $H_2$ gas (Airgas) at a flow rate of ≈160–200 mL $min^{-1}$. The heat treatment involved three separate stages shown in Figure 3: (i) 1 h at 300 °C to remove the PLGA, (ii) 1 h at 600 °C to reduce the metal oxides to metal, and (iii) a sintering stage dependent on the particular metal or alloy composition. Radial cross sections of the samples were mounted in epoxy and polished using standard procedures. Metallic samples were imaged using optical microscopy (Olympus PMG3 inverted metallurgical microscope) on polished cross sections and scanning electron microscopy (Leo Gemini 1525 and Hitachi S3400-II). Energy dispersive spectroscopy was performed on the cross sections coated with 10 nm of Au/Pd (Hitachi S3400-II SEM). Sample dimensions and masses were recorded before and after heat treatment. Porosity was determined using ImageJ image analysis on optical images obtained from polished sample cross sections.

For the redox cycling experiments, ≈10 × 10 mm square samples were cut using a razor blade from larger printed sheets ≈5 mm in height printed using a 200 µm diameter tip advancing at a 120° angle with respect to the previous layer. A 1 mm line spacing was used between the struts. Oxidation cycles were performed in a custom-built steam furnace based on ref.[2]. Samples were heated to 900 °C at a rate of 7.5° $min^{-1}$, held for 3 h, and then furnace cooled. Argon was flowed into a filter flask filled with boiling distilled water. The Ar/steam mixture then flowed through the furnace. Reduction cycles were performed in a hydrogen furnace (MTI Corporation GSL-1500X-50HG) using 99.999% pure $H_2$ gas (Airgas) at a flow rate of ≈160–200 mL $min^{-1}$. Samples were heated to 900 °C at a rate of 10° $min^{-1}$, held for 1 h, and then furnace cooled.

## Supporting Information

Supporting Information is available from the Wiley Online Library or from the author.

## Acknowledgements

A.E.J. and S.L.T. contributed equally to this work. The authors acknowledge use of the following Northwestern University facilities: EPIC Facility (NUANCE Center) supported by NSF DMR-1121262 and EEC-0118025|003 and Optical Microscopy and Metallography Facility supported by NSF DMR-1121262. The authors acknowledge Alexandra L. Rutz for help with creating origami and kirigami samples, Fernando L. Reyes for assistance with metallography, and the laboratory of Prof. T. K. Woodruff for use of their optical microscope. This research was also supported by a gift from Google and funding through the Institute for Sustainability and Energy at Northwestern. A.E.J. was supported by the Department of Defense through the National Defense Science and Engineering Graduate Fellowship and S.L.T. was supported by the NSF Graduate Research Fellowship Program.

Received: September 16, 2015
Revised: September 17, 2015
Published online:

[1] J. M. Torralba, M. Campos, *Rev. Metal.* **2014**, *50*, e017.
[2] G. Sethi, N. S. Myers, R. M. German, *Int. Mater. Rev.* **2008**, *53*, 219.
[3] J. K. Cochran, K. J. Lee, D. McDowell, T. Sanders, presented at *Third Global Symp. Materials Processing and Manufacturing*, Warrendale, PA, February **2002**.
[4] A. Jakus, A. Fredenburg, N. Thadhani, *Mater. Sci. Eng., A* **2012**, *534*, 452.
[5] A. I. C. Ramos, D. C. Dunand, *Metals* **2012**, *2*, 265.
[6] R. Sepúlveda, A. A. Plunk, D. C. Dunand, *Mater. Lett.* **2015**, *142*, 56.
[7] Y. Chino, D. C. Dunand, *Acta Mater.* **2008**, *56*, 105.
[8] M. Chmielus, X. X. Zhang, C. Witherspoon, D. C. Dunand, P. Mullner, *Nat. Mater.* **2009**, *8*, 863.
[9] L. C. Dial, T. H. Sanders, J. K. Cochran, *Metall. Mater. Trans. A* **2012**, *43A*, 1303.
[10] D. D. Gu, W. Meiners, K. Wissenbach, R. Poprawe, *Int. Mater. Rev.* **2012**, *57*, 133.
[11] C. B. Williams, J. K. Cochran, D. W. Rosen, *Int. J. Adv. Manuf. Technol.* **2011**, *53*, 231.
[12] B. G. Compton, J. A. Lewis, *Adv. Mater.* **2014**, *26*, 5930.
[13] Y. X. Gao, H. Y. Li, J. Liu, *PLoS One* **2012**, *7*, e45485.
[14] S. T. Parker, P. Domachuk, J. Amsden, J. Bressner, J. A. Lewis, D. L. Kaplan, F. G. Omenetto, *Adv. Mater.* **2009**, *21*, 2411.
[15] M. J. Xu, G. M. Gratson, E. B. Duoss, R. F. Shepherd, J. A. Lewis, *Soft Matter* **2006**, *2*, 205.
[16] A. E. Jakus, A. L. Rutz, R. N. Shah, unpublished.
[17] A. E. Jakus, E. B. Secor, A. L. Rutz, S. W. Jordan, M. C. Hersam, R. N. Shah, *ACS Nano* **2015**, *9*, 4636.
[18] B. Y. Ahn, D. Shoji, C. J. Hansen, E. Hong, D. C. Dunand, J. A. Lewis, *Adv. Mater.* **2010**, *22*, 2251.
[19] E. Hong, B. Y. Ahn, D. Shoji, J. A. Lewis, D. C. Dunand, *Adv. Eng. Mater.* **2011**, *13*, 1122.
[20] E. Lorente, Q. Cai, J. A. Pena, J. Herguido, N. P. Brandon, *Int. J. Hydrogen Energy* **2009**, *34*, 5554.
[21] K. Otsuka, C. Yamada, T. Kaburagi, S. Takenaka, *Int. J. Hydrogen Energy* **2003**, *28*, 335.
[22] N. Xu, X. Li, X. Zhao, J. B. Goodenough, K. Huang, *Energy Environ. Sci.* **2011**, *4*, 4942.
[23] R. A. Jain, *Biomaterials* **2000**, *21*, 2475.

[24] J. B. Wachtman, *Fabrication of Ceramics*, Ceramic Engineering Society Proceedings, Vol. 14, American Ceramic Society, Westerville, OH, USA **2009**.
[25] H. Hermawan, H. Alamdari, D. Mantovani, D. Dubé, *Powder Metall.* **2008**, *51*, 38.
[26] H. Demars, R. Meyer, *Powder Metall.* **1967**, *10*, 145.
[27] S. Sadighikia, S. Abdolhosseinzadeh, H. Asgharzadeh, *Powder Metall.* **2015**, *58*, 61.
[28] P. Chhillar, D. Agrawal, J. H. Adair, *Powder Metall.* **2008**, *51*, 182.
[29] M. E. Alam, M. Gupta, *Powder Metall.* **2009**, *52*, 105.
[30] G. S. Upadhyaya, *Bull. Mater. Sci.* **2005**, *28*, 305.
[31] S. Chanthapan, A. Kulkarni, J. Singh, C. Haines, D. Kapoor, *Int. J. Refract. Met. Hard Mater.* **2012**, *31*, 114.
[32] K. Wang, X. P. Wang, R. Liu, T. Hao, T. Zhang, C. S. Liu, Q. F. Fang, *J. Nucl. Mater.* **2012**, *431*, 206.
[33] K. Saitou, *Scr. Mater.* **2006**, *54*, 875.
[34] I. M. Fedorchenko, S. M. Solonin, *Powder Metall. Met. Ceram.* **1965**, *4*, 891.
[35] L. M. R. d. Vasconcellos, M. V. d. Oliveira, M. L. d. A. Graça, L. G. O. d. Vasconcellos, Y. R. Carvalho, C. A. A. Cairo, *Mater. Res.* **2008**, *11*, 275.
[36] B. Jiang, N. Q. Zhao, C. S. Shi, X. W. Du, J. J. Li, H. C. Man, *Mater. Lett.* **2005**, *59*, 3333.
[37] G. B. Schaffer, B. J. Hall, *Metall. Mater. Trans. A* **2002**, *33*, 3279.
[38] M. Wolff, T. Ebel, M. Dahms, *Adv. Eng. Mater.* **2010**, *12*, 829.
[39] J. Requies, M. B. Gueemez, S. Perez Gil, V. L. Barrio, J. F. Cambra, U. Izquierdo, P. L. Arias, *J. Mater. Sci.* **2013**, *48*, 4813.
[40] D. Mignard, C. Pritchard, *Int. J. Hydrogen Energy* **2007**, *32*, 5039.
[41] S. Fukase, T. Suzuka, *Appl. Catal. A* **1993**, *100*, 1.
[42] M. Thaler, V. Hacker, A. Anilkumar, J. Albering, J. O. Besenhard, H. Schrottner, M. Schmied, *Int. J. Hydrogen Energy* **2006**, *31*, 2025.
[43] E. Lorente, J. A. Pena, J. Herguido, *Int. J. Hydrogen Energy* **2008**, *33*, 615.
[44] X. Zhao, Y. Gong, X. Li, N. Xu, K. Huang, *J. Electrochem. Soc.* **2013**, *160*, A1241.
[45] X. Zhao, Y. Gong, X. Li, N. Xu, K. Huang, *J. Electrochem. Soc.* **2013**, *160*, A1716.
[46] G. Cesaretti, E. Dini, X. De Kestelier, V. Colla, L. Pambaguian, *Acta Astronaut.* **2014**, *93*, 430.
[47] C. J. Hansen, R. Saksena, D. B. Kolesky, J. J. Vericella, S. J. Kranz, G. P. Muldowney, K. T. Christensen, J. A. Lewis, *Adv. Mater.* **2013**, *25*, 96.
[48] T. M. Devine, J. Wulff, *J. Biomed. Mater. Res.* **1975**, *9*, 151.
[49] N. P. Ziats, K. M. Miller, J. M. Anderson, *Biomaterials* **1988**, *9*, 5.
[50] L. E. Murr, S. M. Gaytan, F. Medina, H. Lopez, E. Martinez, B. I. Machado, D. H. Hernandez, L. Martinez, M. I. Lopez, R. B. Wicker, J. Bracke, *Philos. Trans. R. Soc., A* **2010**, *368*, 1999.
[51] J. Banhart, D. Weaire, *Phys. Today* **2002**, *55*, 37.
[52] M. E. Cates, J. P. Wittmer, J. P. Bouchaud, P. Claudin, *Physical Review Letters* **1998**, *81*, 1841–1844.
[53] A. J. Liu, S. R. Nagel, *Nature* **1998**, *396*, 21–22.